VTT Technical Research Centre of Finland

Thermo-hydraulic performance enhancement of a solar air heater using rotating cylindrical turbulators

Singh, Sarvapriya; Suman, Siddharth; Mitra, Santanu; Kumar, Manish

Published in:
Applied Thermal Engineering

DOI:
10.1016/j.applthermaleng.2023.121748

Published: 05/01/2024

Document Version
Publisher's final version

Applied Thermal Engineering 236 (2024) 121748

Contents lists available at ScienceDirect

Applied Thermal Engineering

journal homepage: www.elsevier.com/locate/apthermeng

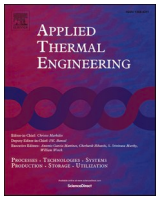

Research Paper

Thermo-hydraulic performance enhancement of a solar air heater using rotating cylindrical turbulators

Sarvapriya Singh [a], Siddharth Suman [b,*], Santanu Mitra [a], Manish Kumar [c]

[a] Department of Mechanical Engineering, Shiv Nadar Institute of Eminence, Tehsil Dadri, UP 201314, India
[b] Centre for Nuclear Safety, VTT Technical Research Centre of Finland, Espoo 02150, Finland
[c] Department of Mechanical Engineering, Malaviya National Institute of Technology, Jaipur 302017, India

ARTICLE INFO

Keywords:
Computational fluid dynamics
Solar energy
Rotating ribs
Cylindrical ribs
Nusselt number
Energy

ABSTRACT

A novel concept of rotating cylindrical ribs as artificial roughness in a solar air heater to enhance its thermo-hydraulic performance factor has been investigated using 3D computational fluid dynamics. The rotational speed is varied from 2000 RPM to 10,000 RPM on the static ribs optimised for height (e), diameter (d), longitudinal pitch (P), and transverse pitch (S) at Reynolds number (*Re*) ranging from 5000 to 24000. The optimised static ribs configuration having e = 3.5 mm, d = 3 mm, S = 20 mm, and $P/e = 10$ is experimentally validated to establish the accuracy of rotating ribs performance computed using computational fluid dynamics. The maximum thermo-hydraulic performance factor of 1.89 is achieved—32 % higher than the best performance for static ribs—using rotational ribs for the rotational speed of 10,000 RPM at $Re = 5000$. A comparison between parallel and perpendicular orientations of rotating ribs with respect to the absorber plate establishes that perpendicular ribs configuration is highly desirable to reduce the pressure drop penalty, in turn, enhancing the thermo-hydraulic performance. The performances of the proposed perpendicularly oriented rotating cylindrical ribs are also compared with the performances reported in the literature for static ribs of different shapes having the same orientation with respect to absorber plate and it is observed that rotational ribs outperforms all the other static ribs.

1. Introduction

The global phenomenon of climate change has compelled humanity to shift its focus from conventional energy sources toward renewable alternatives. Consequently, an urgent necessity in the current circumstances is to phase out the production and consumption of fossil fuels in order to fulfill the worldwide energy demand. Capitalizing on the immense potential of renewable energy sources, there has been a notable emphasis on converting them into practical or useful energy in recent times. Solar energy and wind energy are the forefront in utilization among all renewable energy sources. This is due to their widespread availability and abundance in nature across nearly all geographical locations on Earth [1]. Solar energy constitutes the most easily accessible form of renewable energy. Approximately 60 % of the rise in global renewable power capacity is attributed to the utilization of solar energy, marking a 25 % increase from the previous year's figures [2–4].

One of the most widely employed methods of harnessing solar energy and transforming it into practical use involves converting it into thermal energy using solar thermal collectors. These collectors have gained considerable popularity for routine tasks due to their simple design, minimal maintenance requirements, and user-friendly operation. Solar thermal collectors can be classified into two main categories: solar water heaters (SWH) and solar air heaters (SAH), based on the type of fluid flowing within the pipes or ducts. In the context of the present discussion, the focus is directed toward solar air heaters (SAH) due to their wide-ranging applications in various domains. These applications include space heating, timber seasoning, and the drying of food grains among others. The versatility of SAH systems makes them an invaluable asset in addressing diverse energy needs and practical requirements.

The thermal efficiency of conventional SAH systems having smooth absorber plate is considerably low, primarily due to the inherent poor thermal conductivity of air and the formation of a viscous sublayer at the absorber plate [5,6]. This sublayer forms beneath the absorber plate impedes the heat transfer to the flowing fluid within the duct. Consequently, the average wall temperature of the absorber plate increases, leading to radiation losses to the surrounding environment. To mitigate

* Corresponding author.
E-mail address: siddharth.suman@vtt.fi (S. Suman).

https://doi.org/10.1016/j.applthermaleng.2023.121748
Received 15 January 2023; Received in revised form 21 August 2023; Accepted 4 October 2023
Available online 5 October 2023

this, it becomes imperative to disrupt the formation of the viscous sublayer by implementing certain technique beneath the heated absorber plate. Introducing artificial roughness having different shapes and sizes is the most economical approach to disrupt the formation of the viscous sublayer. However, the presence of these artificial ribs leads to a reduction in the cross-sectional area available for fluid flow in the test section causing a subsequent pressure drop across the test section. This necessitates a balance between enhancing the overall thermal efficiency and minimizing the increase in pressure drop across the test section.

The concept of introducing roughness to the inner surface of pipes was first explored by Nikuradse [7]. He applied uniformly sized particles of building sand to create roughness on the wetted surface of circular tubes, aiming to investigate fluid flow behavior under fully turbulent conditions. His observations revealed that this artificial roughness induced turbulence in the vicinity of the roughened wall. Building on Nikuradse's concept of roughening the inner surface of circular pipes, Webb et al. [8] conducted an experimental study to delve into the characteristics of heat transfer and fluid flow when ribs were repeatedly added to create roughness in turbulent pipe flow. In their study, they derived correlations for the friction factor, taking into account the relative roughness pitch (P/e), a factor that had been overlooked in previous research. Additionally, they emphasized the significance of the Prandtl number within the heat transfer correlation, in contrast to earlier studies. They argued against employing a single correlation for different roughness geometries. Consequently, Webb et al. [9] performed a comparative analysis of generalized correlations for heat transfer and friction characteristics alongside other roughness geometries. Their findings indicated that friction factor values were 7 % lower when circular ribs were used compared to square-edged ribs. However, minimal impact was observed on heat transfer characteristics when different roughness geometric topologies were tested within similar geometric parameters. Webb and Eckert [10] extended the application of these developed correlations to heat exchanger design across three scenarios: reduced heat transfer area, increased heat transfer capacity, and decreased frictional power consumption. They presented a comprehensive expression involving the ratios of Stanton number and friction factor for all three cases. Particularly noteworthy was the expression addressing increased heat transfer capacity while maintaining equal pumping power, which emerged as a valuable formula for comparing any roughened duct with a smooth one.

Previous studies have highlighted the superior performance of circular-sectioned ribs in terms of friction factors. Consequently, several early investigations have been conducted by various researchers using small-diameter cylindrical wires to introduce artificial roughness to one broad wall of rectangular SAH ducts [11–14]. Table 1 provides a summary of these research work focused on SAH roughened with artificial roughness. Prasad and Mullick [11] studied the impact of protruding wires on smooth galvanized iron sheets and corrugated sheets, noting an enhancement in the heat transfer coefficient due to the presence of small-diameter wires. Similarly, Prasad and Saini [12] investigated SAH ducts roughened with small-diameter wires to analyze the effects of parameters such as relative roughness height (e/D_h), relative roughness pitch (P/e), and Reynolds number. They discovered that as e/D_h value increased, the heat transfer rate decreased while the friction factor rate increased. Furthermore, an increase in P/e value resulted in decreased heat transfer and friction factor rates. Gupta et al. [13] performed an experimental study in the transitionally rough flow region to assess the impact of e/D_h and Re, with $P/e = 10$, on heat transfer and fluid flow characteristics across various aspect ratios of rectangular roughened SAH ducts. They concluded that heat transfer behavior differs between the transitionally rough flow region and the fully rough flow region. These findings bear significant relevance for solar thermal applications, as a substantial portion of SAH systems operate within this regime. Subsequently, Verma and Prasad [14] carried out an experimental investigation to identify optimal thermo-hydraulic performance by simultaneously considering the effects of e/D_h and P/e in the transitionally rough flow region. Their research revealed an optimal thermo-hydraulic performance of 71 % at $e^+ = 24$, which is the function of roughness and flow parameters. In summary, the articles discussed collectively indicate that the placement of artificial roughness beneath the absorber plate enhances heat transfer. However, this technique also contributes to a drop in fluid pressure along the direction of flow within the test section. To mitigate this pressure-drop penalty to some extent, researchers have implemented a discrete arrangement of artificial ribs perpendicular to the absorber plate. Furthermore, Gawande et al. [15] provided a comprehensive review of the CFD methodology for optimizing roughness parameters to achieve maximum thermo-hydraulic performance factor (THPF). They emphasized its applicability even prior to conducting experimental investigations, as a means to comprehend heat transfer and fluid flow characteristics when implementing novel roughness arrangements within roughened SAH systems. Manjunath et al. [16] combined a CFD investigation with experimental validation on smooth ducts, focusing on the impact of spherical turbulence generators for enhancing heat transfer from the absorber plate and fluid flow characteristics. They observed significant influence from the ratios P/D and the spherical ball size (D) on heat transfer and fluid flow characteristics. The highest heat transfer enhancement, 2.52 times over a smooth plate, was achieved at $P/D = 3$ and D = 25 mm with $Re = 23560$. However, this enhancement came with a pumping power penalty, which was most prominent at lower P/D and higher D values at $Re = 23560$. Further, to evaluate turbulence generator performance, Manjunath et al. [17] conducted a CFD investigation with arrays of pin fins. They found that larger fin diameters and shorter pitchs yielded higher thermal efficiency. The pin fin arrangement outperformed spherical turbulence generators within a lower Reynolds number regime up to $Re = 13500$ but lost its advantage afterward in terms of overall heat transfer enhancement. Other geometries such as stepped cylindrical turbulence generators [18], helicoidal spring-shaped fins [19], and vertical coil springs [20] were also explored to understand their effects on heat transfer and fluid flow characteristics within SAH systems.

Although several studies examined discrete vertical ribs to comprehend their impact on the overall thermal performance of roughened SAH systems while considering various parameters, these studies often utilized a fixed transverse pitch (S) value, which could be an influential parameter [16–20]. However, a recent study investigating transverse pitch focused on square ducts, had the aspect ratio not recommended for SAH applications [21]. To fill this research gap, there is a need for a detailed investigation involving the vertical orientation of the artificial roughness and its impact on thermal performance while considering the role of horizontally oriented transverse ribs. Additionally, the phenomenon of re-circulation zones forming behind fixed artificial ribs, leading to hotspots near the absorber plate, has been reported by numerous researchers [22–27]. These hotspots can adversely affect heat transfer, thereby increasing convective and radiative losses to the environment. Consequently, the exploration of a novel technique to mitigate re-circulation zones through the rotation of artificial ribs to enhance heat transfer performance has garnered attention in review articles [28,29]. This novel technique warrants further exploration to evaluate its feasibility and potential benefits, this is the focus of this research work.

Based on the literature review concerning SAH systems enhanced through artificial roughness, it is evident that arranging discrete artificial ribs perpendicular to the absorber plate effectively enhances heat transfer while simultaneously minimizing pressure drop across the test section. However, the impact of the transverse pitch of discrete ribs has not been investigated in detail. Therefore, this study focuses on vertical cylindrical ribs oriented perpendicular to the absorber plate, investigating the effects of geometrical parameters: roughness height (e), roughness diameter (d), roughness longitudinal pitch (L), and roughness transverse pitch (S)), and their arrangement in both the longitudinal and transverse directions. This investigation aims to provide insights into

Table 1
A summary of the research works for SAH roughened with artificial roughness.

Ref.	Range of parameters	Rib shape and arrangement	Investigation	Findings
[8]	$e/D_h = 0.01–0.04$, $P/e = 10–40$, $Pr = 0.71–37.6$, $Re = 6000–100000$	Repeated rectangular ribs	Experimental & Analytical	The highest heat transfer was achieved at $e/D_h = 0.04$ and $P/e = 10$, corresponding to a lower Re value. Furthermore, the friction factor also reached its maximum at these specific conditions.
[10]	$e/D_h = 0.01–0.04$, $P/e = 10$, $Pr = 0.71–37.6$, $Re = 6000–100000$	Repeated rectangular ribs	Experimental & Analytical	Under heat flux operating condition, the expression for increasing heat transfer capacity while maintaining equal pumping power is as follows: $\frac{K}{K_s} = \frac{\frac{St}{St_s}}{(\frac{f}{f_s})^{\frac{1}{3}}}$
[11]	$e/D_h = 0.019$, $P/e = 15.12$, H = 25.4 mm, W = 141 mm, $Re = 10000–40000$	Repeated protruding wires	Experimental	At $Re = 20000$, there was a 44.5 % enhancement in plate factor efficiency compared to the corrugated plate. Improvements were more pronounced at lower velocities.
[12]	$e/D_h = 0.02–0.033$, $P/e = 10–20$, $Re = 5000–50000$	Small-diameter protruding wires	Experimental	With lower value of P/e, reattachment may not occur, leading to a reduction in heat transfer.
[13]	$e/D_h = 0.018–0.052$, $P/e = 10$, W = 150 mm, $W/H = 6.8–11.5$, $Re = 3000–18000$	Transverse wires	Experimental	The heat transfer and friction factor correlations were found to be influenced by the aspect ratio, albeit to a lesser degree.
[14]	$e/D_h = 0.01–0.03$, $e^+ = 8–42$, $P/e = 10–40$, $Re = 5000–20000$	Small diameter wires	Experimental	The Nusselt number enhancement ratio (Nu_r/Nu_s) was found in the range of 1.25–2.08 over the smooth duct.
[16]	D = 5–25 mm, P = 60–240 mm, $P/D = 3–12$, $Re = 4000–25000$, S = 37.5 mm, W = 150 mm, $W/H = 6$	Spherical turbulence generators	Experimental & CFD (Fluent)	With $P/D = 3$ and D = 25 mm, an average thermal efficiency increase of 23.4 % over the smooth duct was achieved. Additionally, the peaks of the Nusselt number were observed on the upstream surface of the spherical turbulators.
[17]	$D_w = 1–2.2$ mm, H = 30 mm, $L_w = 30$ mm, P = 30–50 mm, $Re = 4000–24000$, S = 12.5 mm, W = 150 mm	An array of pin fins	CFD (Fluent)	$D_w = 2.2$ mm and L = 30 mm resulted in an average thermal efficiency increase of 14.2 % compared to the smooth duct.
[18]	d = 3–7 mm, H = 30 mm, n = 1–3, $P/h = 11.11–27.78$, $Re = 3000–24000$, s = 1–3, S = 50 mm, W = 200 mm	Stepped cylindrical turbulence generators	CFD (Fluent)	The maximum THPF of 1.27 was obtained for $P/h = 22.22$, s = 3, n = 3, and d = 7 mm at $Re = 4000$.
[19]	$d/H = 0.0533–0.1067$, $D/W = 0.02–0.12$, h = 25 mm, H = 30 mm, n = 2, $P_s/H = 0.1–0.167$, P = 200 mm, $Re = 3000–24000$, S = 100 mm, W = 200 mm	Helicoidal spring-shaped fins	Experimental & CFD (Fluent)	The maximum THPF of 1.268 was obtained at $Re = 3000$ for $D/H = 0.06$, however, $D/H = 0.04$ outperformed other arrangements until $Re = 15000$. Furthermore, the values were found similar after $Re = 15000$ for $D/H = 0.04$ and 0.02.
[20]	$d_c = 10–20$ mm, $d_w = 0.5–2$ mm, $h_c = 3–9$ mm, H = 25 mm, $p_c = 1–3$ mm, $Re = 5867–23471$, P = 42 mm, S = 30 mm, W = 150 mm	Vertical coil springs	Experimental	The highest performance index of 2.98 was achieved for $d_c = 10$ at $Re = 23471$.

(continued on next page)

Table 1 (*continued*)

Ref.	Range of parameters	Rib shape and arrangement	Investigation	Findings
[21]	$d/H = 0.02–0.06$, $e/H = 0.02–0.06$, $L/H = 0.1–0.5$, $S/H = 0.1–0.5$, $Re = 5000–18000$, W = 50 mm, $W/H = 1$	Cylindrical shape rib	CFD (Fluent)	The highest THPF value of 1.2 was attained at $Re = 12000$ for $d/H = 0.055$, $e/H = 0.053$, $L/H = 0.192$, and $S/H = 0.158$.

fluid dynamics that contribute to enhanced heat transfer from the absorber plate across a Reynolds number range spanning from 5000 to 24000. In essence, a detailed parametric optimization is conducted through CFD simulations to maximize the thermo-hydraulic performance factor (THPF). Furthermore, the optimized configurations of the rib roughness are examined to understand the implications of introducing rotating ribs on the thermal performance of the SAH system. The ribs are subjected to rotation, varying between 2000 and 10,000 RPM, to explore the potential benefits and feasibility of this approach.

2. Numerical analysis

Numerical investigation of the 3-D computational fluid domain of roughened SAH duct is carried out in commercial software named ANSYS fluent Research 2021 R2 code. The procedure from geometry creation to the results post-processing is discussed in the subsequent subsections.

2.1. Geometric details

Solar air heater consists mainly of three sections: incoming, test, and outgoing. The test section carries an absorber plate at the top where the uniform heat flux is supplied. Artificial roughness is used to roughen the test section on the fluid-flowing side. Vertical cylindrical ribs are attached underneath the absorber plate on the fluid-flowing side. The arrangement of the ribs used for investigation is shown in Fig. 1. The geometric details of the roughened test section are provided in Table 2. Fluid enters through the incoming section and exits through the outgoing section. It has been observed in earlier studies that the fluid flow becomes periodic after the first three or four ribs interaction in the test section; therefore, to reduce the computational time of the analysis, a periodic domain of one pitch is considered for the CFD analysis [22,24,26]. The periodic domain consisting of vertical cylindrical ribs with in-line arrangement varies with different geometric values. Apart from the longitudinal pitch, the ribs also vary in the transverse direction.

Table 2
Geometric details of roughened test section used for CFD simulation.

Parameters	Values
Duct aspect ratio (W/H)	12
Height of duct (H)	25 mm
Hydraulic diameter (D_h)	46.154 mm
Test section length (L_2)	1000 mm
Rib height (e)	1.5 mm, 2 mm, 2.5 mm, 3 mm, 3.5 mm
Rib diameter (d)	3 mm, 4 mm, 5 mm, 6 mm
Relative roughness pitch (P/e)	8–14
Rib transverse pitch (S)	15 mm, 20 mm, 30 mm, 40 mm, 50 mm, 100 mm

2.2. Discretization of the computational domain

The present computational periodic fluid domain is created in the ICEM CFD package provided in ANSYS academic license 17.2. Required points are generated to make the curves through them, and further curves are modified into surfaces. Vertical cylindrical bodies are defined as solid bodies, whereas the rest of the computational domain is defined as fluid. The solid bodies are blocked individually to control the

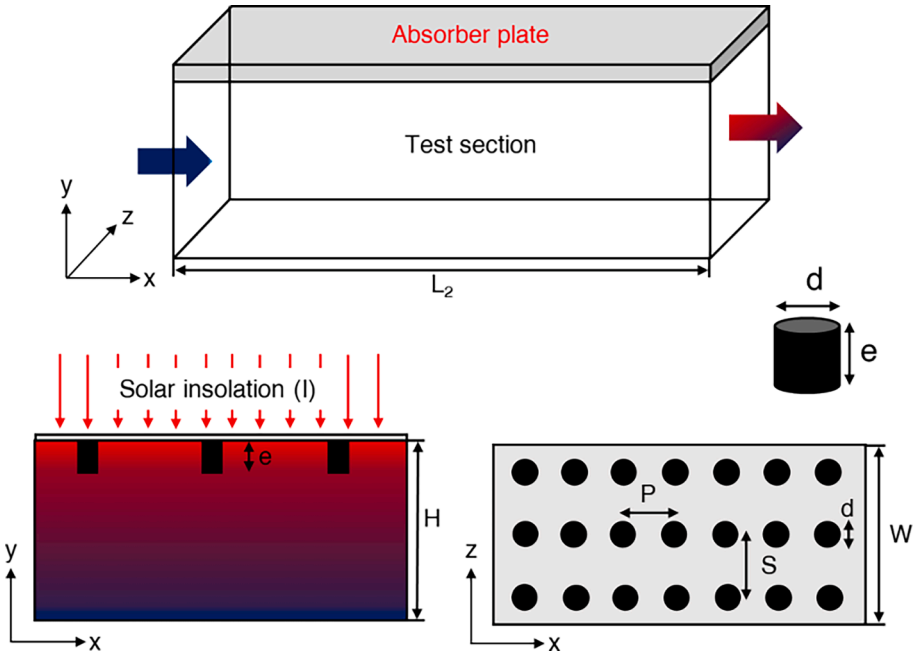

Fig. 1. Schematic of roughened SAH with vertical cylindrical ribs.

discretization around them. The considered computational domain is discretized into small elements/volumes—structured non-uniform cells. Around the vertical cylindrical bodies, it has been ensured that a y + value equal to one should be maintained. Based on this value, the first layer thickness is calculated near the walls. The geometric distribution function with a growth rate of 1.1 inflates the layers, and at least 15 layers are considered around solid bodies.

2.3. Physical modeling

To get the convergence of Reynolds' Average Navier-Stokes (RANS) equations, the present computational domain is discretized into small volumes/elements. The finite volume method (FVM) is used to solve the equations. To keep the check between accuracy and the less computational time, some well-established assumptions are taken into consideration for the present CFD analysis and are given as follows:

- Thin wall model is applied for solid walls of the SAH because the Biot number is calculated below 0.01.
- The fluid flow is considered incompressible in nature.
- 3-D CFD analysis is performed in a steady state for fixed ribs and transient for rotating ribs.
- The thermo-physical properties are considered constant throughout the analysis.
- Radiation is not considered during the simulations.

2.4. Boundary conditions

The considered computational fluid domain is specified with the required boundary names in the ICEM CFD package during the discretization. The inlet is defined to induct fluid flow at one face, while the outlet is specified to outflow the fluid. The wall boundary type introduces the other faces of the duct. The interior kind of boundary condition defines the fluid domain, while the cylindrical bodies are mentioned as solid bodies. After importing the mesh file in the fluent solver, text user interface (TUI) commands are executed in the ANSYS fluent console window to redefine the default velocity inlet and outflow boundary condition to periodic translational condition and periodic shadow at the inlet and the outlet, respectively. Text commands are executed successfully to define translational periodicity at the inlet whereas the outflow type boundary condition at the outlet is permanently deleted while executing the TUI commands, which functions automatically as a periodic shadow. Constant mass flow rate is provided at the inlet corresponding to the required *Re* value. The range of operating parameters used in the present CFD analysis is given in Table 3. A Uniform heat flux of 1000 W/m^2 is applied on the absorber plate of SAH, whereas walls other than the absorber plate are considered insulated. The thermophysical properties of an absorber plate and flowing fluid are tabulated in Table 4. The no-slip boundary condition is ensured near the walls of the SAH.

2.5. Numerical solution methodology

Double precision pressure-based solver with absolute velocity formulation is chosen for CFD analysis. Equations of conservation of mass (Eqn. (1)), momentum (Eqn. (2)), and energy (Eqn. (3)) are solved

Table 3
Operating parameters used for present numerical analysis.

Parameters	Range
Mass flow rate ($\dot{m}$)	0.0151 Kg/s–0.0724 Kg/s
Prandtl number (*Pr*)	0.708
Reynolds number (*Re*)	5000–24000
Uniform heat flux (I)	1000 W/m^2

Table 4
Thermophysical properties of the absorber plate and the working fluid.

Properties	Aluminium (Absorber plate)	Air (Working fluid)
Density (ρ)	2719 Kg/m^3	1.165 Kg/m^3
Dynamic viscosity (μ)	–	1.8566 × 10^{-5} N/m^2-s
Specific heat (c_p)	871 J/Kg-K	1006.96 J/Kg-K
Thermal conductivity (k)	202.4 W/m-K	0.0264 W/m-K

in commercial software named ANSYS Fluent™ code 2021 R2 research license.

$$\nabla \bullet (\rho \bullet \vec{v}) = 0 \tag{1}$$

$$\nabla \bullet (\rho \bullet \vec{v} \bullet \vec{v}) = -\nabla p + \nabla \bullet \left(\mu \left[\left(\nabla \vec{v} + \nabla \vec{v}^{\hat{A}}\right) - \frac{2}{3}\nabla \bullet \vec{v} I\right]\right) \tag{2}$$

$$\nabla \bullet (\vec{v}(\rho E + p)) = \nabla \bullet \left(k_{eff}\nabla T - h\vec{J} + \left(\mu\left[\left(\nabla \vec{v} + \nabla \vec{v}^{\hat{A}}\right) - \frac{2}{3}\nabla \bullet \vec{v} I\right].\vec{v}\right)\right) \tag{3}$$

The scheme of the SIMPLE (Semi-Implicit Method for Pressure-Linked Equations) is applied for pressure-velocity coupling. Least squares cell-based discretization for the gradient is chosen. Pressure components are solved by second-order discretization. Similarly, a second-order upwind scheme for momentum, turbulent kinetic energy, and dissipation rate is applied to solve the governing equations in the numerical solution. To control the solution, default under-relaxation factors are considered for the present investigation throughout the analysis. To get the convergence of the current numerical solution, residual absolute criteria for mass, momentum, turbulence model terms, and energy are set to achieve order below 10^{-5}, 10^{-6}, 10^{-6}, and 10^{-8}, respectively.

2.6. Procedure to calculate THPF

Reynolds number at the inlet is defined by,

$$Re = \frac{\rho D_h V}{\mu} \tag{4}$$

The average convective heat transfer coefficient is defined by,

$$h_{avg} = \frac{1}{A}\int hdA \tag{5}$$

The average Nusselt number is calculated by,

$$Nu_{avg} = \frac{h_{avg} \times D_h}{k_{air}} \tag{6}$$

The hydraulic diameter at the inlet is calculated as,

$$D_h = \frac{4A_c}{P_{wetted}} \tag{7}$$

The friction factor is defined as,

$$f_r = \frac{\left(\frac{\Delta P}{L_2}\right) \times D_h}{2\rho v^2} \tag{8}$$

Thermo-hydraulic performance factor (THPF) [10] is defined by,

$$THPF = \frac{(Nu_r/Nu_s)}{(f_r/f_s)^{1/3}} \tag{9}$$

3. Experimental study

3.1. Experimental test rig details

A pictorial view of the experimental test rig is provided in Fig. 2. It contains three sections: inlet, outlet, and test. The lengths of the inlet and outlet sections are considered as per ASHRAE standards [30,31]. The inlet section is 500 mm long whereas the outlet section is 250 mm long, more than $5\sqrt{W \times H}$ and $2.5\sqrt{W \times H}$, respectively. The sections of the rectangular duct are fabricated with acrylic glass because of their smooth surface and poor thermal conductivity. The individual walls are glued with acetone to form the closed rectangular duct. Thus, the acetone is poured into the joints with an injection needle to ensure the connections air leakproof. It took around 15 min to settle down at room temperature and made formidable joints. An absorber plate made of Aluminium having 6 mm thickness is attached at the top of the test section. The distinct cross-sectional areas are connected with transition zones which are 3-D printed with Polylactic acid (PLA) filament material—thermoplastic polyester. The outlet pipe contains the orifice meter coupled with a U-tube manometer and control valve. The U-tube manometer with an orifice plate calculates the duct's mass flow rate, whereas a control valve controls the flow rate. At the end, the centrifugal blower's inlet section is connected to the outlet pipe with the help of a transition zone. The centrifugal blower sucks the air at the inlet of the rectangular duct, where a honeycomb structure is attached to the rectangular duct at the inlet for air to enter the duct with the least effort. The absorber plate is heated up with the help of mica flat plate heaters connected to the power transformer to control the desired power input. The ammeter and voltmeter are associated with the power supply to indicate the input voltage provided to the absorber plate. The mica flat plate heaters are connected in parallel and series combinations to achieve the required heat flux. The upper surfaces of the heaters are well insulated with Aluminium silicate high-temperature insulation ceramic fibre blanket of the covering area more than the absorber plate area. The roughened absorber plate carries 3-D printed optimized cylindrical ribs, which are attached with the help of Araldite epoxy adhesive—it took 48 h to settle at the particular places adequately at room temperature. Calibrated copper-constantan K-type thermocouples are used to capture the transient temperature readings and recorded by the data acquisition system connected with the computer carrying the software to display the electronic data into the actual numerical values. The experimental test rig is mounted on the foundation provided with the thermocol sheets below the test section which helps in maintaining equal levels between the rectangular duct's inlet and the inlet of the centrifugal blower.

3.2. Experimental procedure

Before getting the readings from the experimental test rig, the test is run to achieve a steady flow rate. It took around 2.5 h to achieve a steady state for each run. A total of six runs are performed to get the data for the required range of Reynolds numbers, and each run is performed at least twice to ensure repeatability. The following data are extracted for each run:

- The mass flow rate at the inlet to get the required *Re*

$$\dot{m} = \rho A_c V \tag{10}$$

- The temperature readings at the outlet and the inlet

A total of six thermocouples are fixed at the inlet and outlet. Therefore, the arithmetic mean of three thermocouples is used to calculate the mean T_i and T_o.

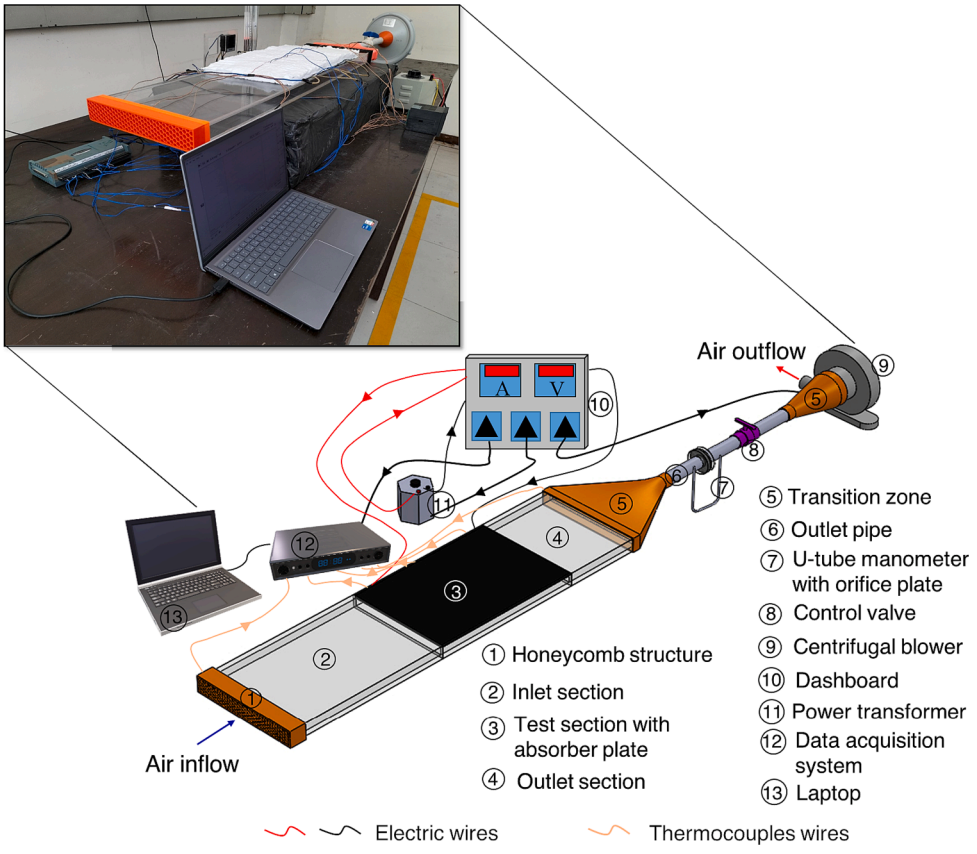

Fig. 2. A pictorial view of the experimental test rig, and its schematic.

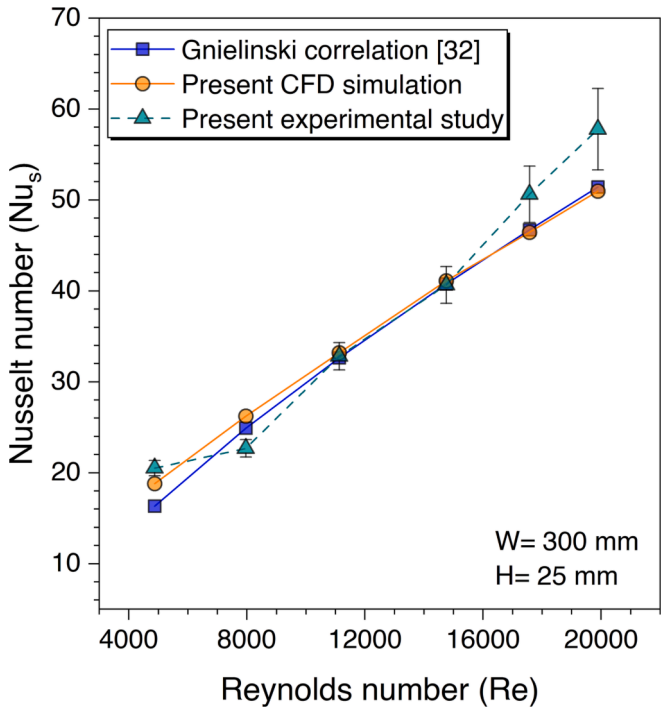

Fig. 3. Smooth duct validation, Nu_s vs *Re*.

$$T_i = \frac{(T_{c1} + T_{c2} + T_{c3})}{3}, T_o = \frac{(T_{c4} + T_{c5} + T_{c6})}{3} \tag{11}$$

- Total heat absorbed by the fluid which is calculated as

$$Q_g = \dot{m} c_p (T_o - T_i) \tag{12}$$

- The temperature readings at the absorber plate

A total of ten thermocouples are used to record the absorber plate temperature, and the average wall temperature is the arithmetic of all ten thermocouples.

$$T_w = \frac{(T_{c7} + T_{c8} + T_{c9} + T_{c10} + T_{c11} + T_{c12} + T_{c13} + T_{c14} + T_{c15} + T_{c16})}{10} \tag{13}$$

These readings are used to calculate the average convective heat transfer coefficient, and further, the Nusselt number values are computed on each *Re* value.

4. Results and discussion

A detailed investigation is carried out to showcase the concept of rotating turbulators in a roughened SAH. The investigation progressed from the smooth duct validation to the CFD parametric optimization of the vertical cylindrical ribs and presents the effects of the rotating turbulators with optimized dimensions on the thermal performance of roughened SAH.

4.1. Smooth duct validation

Even though there are multiple theoretical correlations exist in the literature for smooth ducts, however, the Gnielinski correlation fits the most for the SAH operating regime [32]. The smooth duct of an aspect ratio equal to twelve is created and discretized in the ICEM CFD package. In addition, an experimental study is also carried out with the same dimensions as of numerical study. The variation of Nu_s values against *Re* is shown in Fig. 3. The correlation values are observed to agree with the CFD numerical and experimental values. The experimental values are plotted with the uncertainty associated with each value with an error bar. The uncertainty details are provided in **Appendix A**.

Gnielinski correlation: $Nu = \frac{\left[\left(\frac{f}{8}\right)(Re-1000)Pr\right]}{\left[1+12.7\sqrt{\left(\frac{f}{8}\right)}\left(Pr^{\frac{2}{3}}-1\right)\right]}$

$$f = [0.79\ln(Re) - 1.64]^{-2}; 2300 < Re < 10^6; 0.5 < Pr < 2000 \tag{14}$$

Similarly, the friction factor values of smooth duct are validated with the Bhatti and Shah correlation [33]. The variation of friction factor values is carried out for *Re* ranges 5000–24000. The variation is plotted in

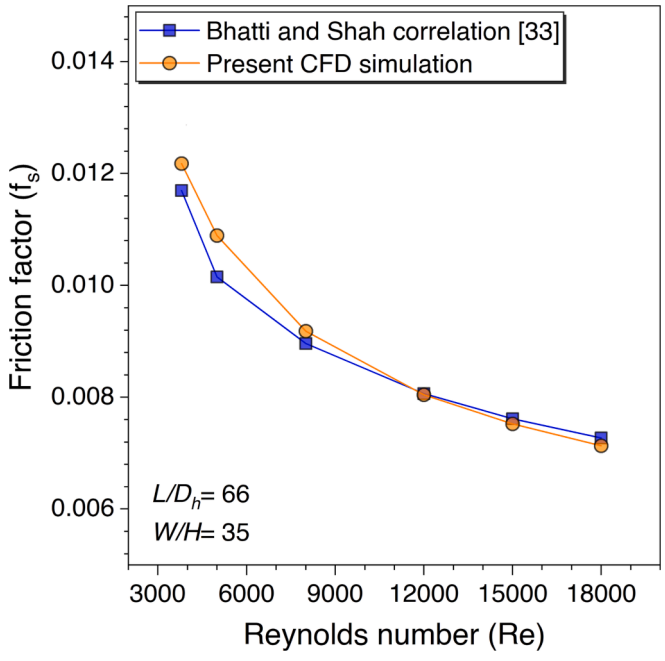

Fig. 4. Smooth duct validation, f_s vs Re.

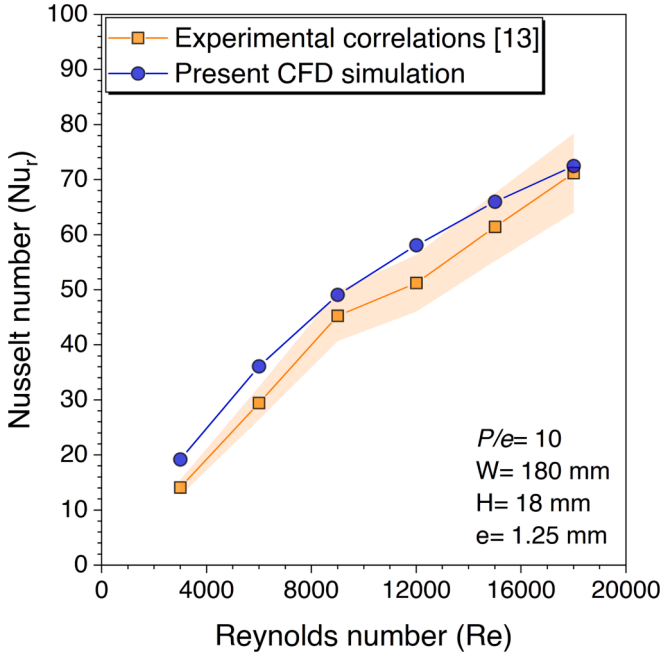

Fig. 5. Roughened duct validation, Nu_r vs Re.

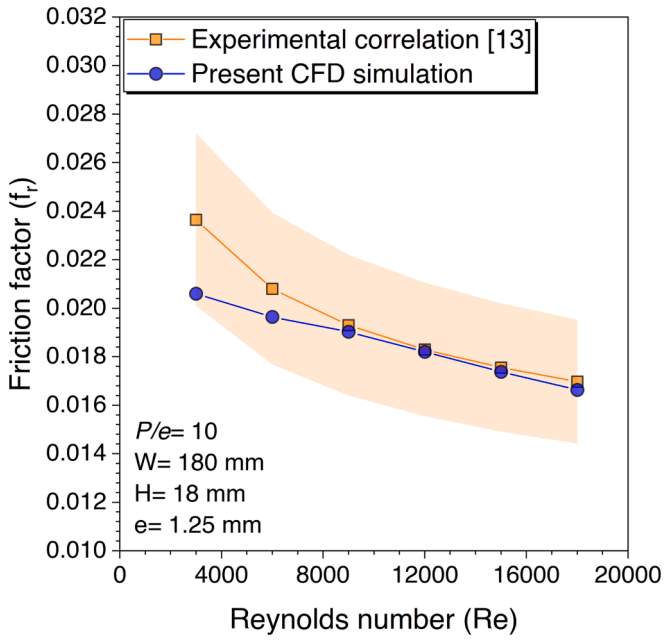

Fig. 6. Roughened duct validation, f_r vs Re.

Fig. 4. The CFD values are observed to agree with the Bhatti and Shah correlation values.

Bhatti and Shah Correlation:

$$f = \left(1.0875 - 0.1125\frac{H}{W}\right) f_c$$
$$f_c = 0.0054 + 2.3 \times 10^{-8}\, Re^{1.5};\ 2300 < Re < 4000 \quad (15)$$
$$= 1.28 \times 10^{-3} + 0.1143\, Re^{-0.311};\ 4000 < Re < 10^7$$

4.2. Roughened duct validation

A validation of roughened duct is performed considering a duct having an aspect ratio of ten and $P/e = 10$. Correlations for roughened ducts with transverse cylindrical wires were developed by conducting experiments based on different aspect ratio values and the relative roughness height for a *Re* range of 3000–18000 [13]. Numerical results are generated by considering the geometric parameters within the range given for the developed correlations. The variation in the Nu_r values against *Re* is shown in Fig. 5. The experimental values are plotted with the error band provided for the experimental correlations. It can be seen from Fig. 5 that the numerical values are observed to be an excellent match to the experimental correlations predicted values.

Likewise, the validation of roughened duct for f_r values is also conducted. The experimental correlation values are plotted in Fig. 6 with the error band provided with the developed correlation for the friction factor. CFD simulations are performed for *Re* ranging from 3000 to 18000. The numerical values are found to be an excellent match to the experimental correlation values except $Re = 3000$. This is because the turbulence model used to simulate the computational fluid domain does not predict the results perfectly, as this *Re* value lies in the transition flow zone.

4.3. Parametric optimization of geometric parameters

As indicated by the literature review, the enhancement of thermal performance in roughened SAHs is heavily influenced by the geometric dimensions and positioning of ribs. Therefore, the effects of different geometric parameters and their placement are discussed in the subsequent subsections in detail.

4.3.1. Grid sensitivity analysis

In order to ensure the numerical results are unaffected by grid resolution, a grid sensitivity analysis is conducted for SAH roughened with vertical cylindrical ribs. The grid density varies from 789,404 to 4,308,344 nodes to discretize the computational fluid domain. The variation of Nu_r and f_r values are plotted in Fig. 7 against the number of nodes. It has been observed from the plot that the percentage change in both the parameter values is found to be less than 1 % after the number of nodes equal to 2,058,600 with two consecutive grid density resolutions. Hence, this grid resolution was used for discretizing the present computational fluid domain in subsequent analyses.

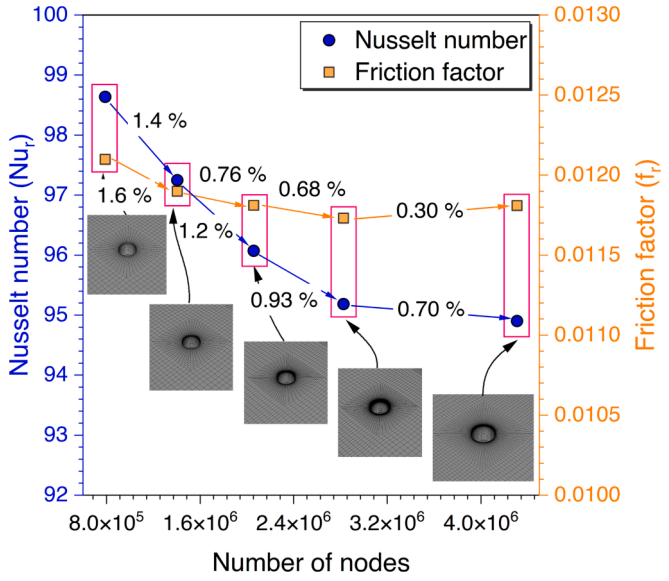

Fig. 7. Grid sensitivity analysis.

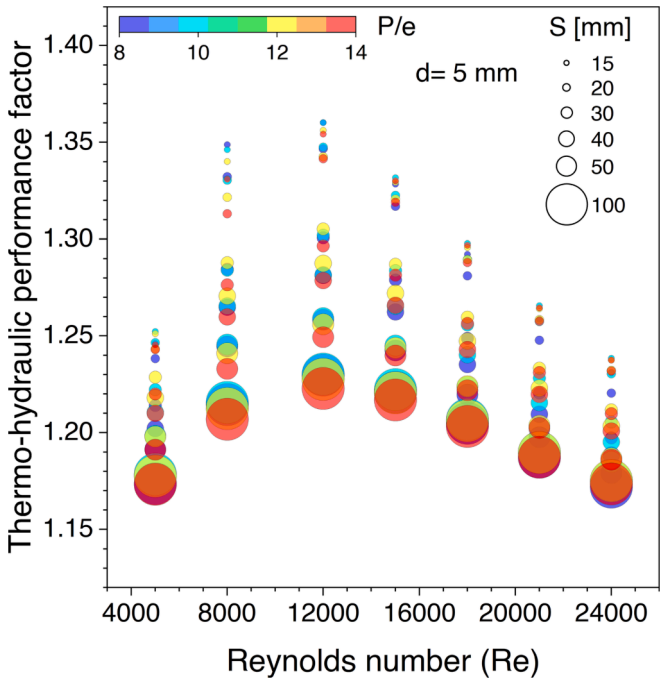

Fig. 8. The variation in the THPF values for different values of P/e.

4.3.2. Effects of relative roughness pitch (P/e)

Longitudinal pitch is reported by almost all researchers in studying any new arrangement of artificial ribs in a roughened SAH with the periodic domain. Therefore, the effects of the longitudinal pitch reported in relative roughness pitch (P/e) are first carried out to study the concept of vertical cylindrical ribs. The P/e value for investigation varies from 8 to 14, while the other geometric parameters of the cylindrical ribs are considered constant. In addition, placement of the ribs in the transverse direction varies from 15 to 100 and is designated by the letter 'S'. Thus, the variation of THPF values against the Reynolds number for different values of the relative roughness pitch and the transverse pitch is plotted in Fig. 8. It can be observed from the plot that the values reach their maximum at $Re = 12000$ and begin to decrease as the Reynolds number increases. A similar trend is observed for all the investigated values of the transverse pitch.

It is observed from Fig. 8 that the $P/e = 10$ gives the maximum THPF values for all the investigated ranges of the Reynolds number. The maximum THPF is yielded 1.36 for $P/e = 10$, S = 15 mm at $Re = 12000$. This is because the space between two straight ribs with $P/e = 10$ is sufficient to re-attach the fluid particles to the absorber plate surface after separating from the cylindrical surface and simultaneously detaching from the region—extracting the maximum heat from the absorber plate. However, this continuous process is not happening with other values of P/e, which means either the fluid particles are not getting the space reaching the absorber plate surface to re-attach or re-attaching long to the absorber plate surface with P/e values above ten, resulting in less heat transfer. Hence, $P/e = 10$ is concluded as the optimum condition for further analyses.

To support the reasoning of separation and re-attachment process on the overall performance of a present roughened duct, the path lines coloured by velocity magnitudes for different values of P/e are illustrated in Fig. 9. The path lines are plotted on a plane at 1 mm below the absorber plate to understand the fluid flow behaviour around a cylinder. Upon impact with the cylindrical bodies, fluid particles become separated and subsequently move around these bodies due to retained momentum. The separated fluid particles converge with those situated behind the cylindrical body in the downstream region. Notably, these

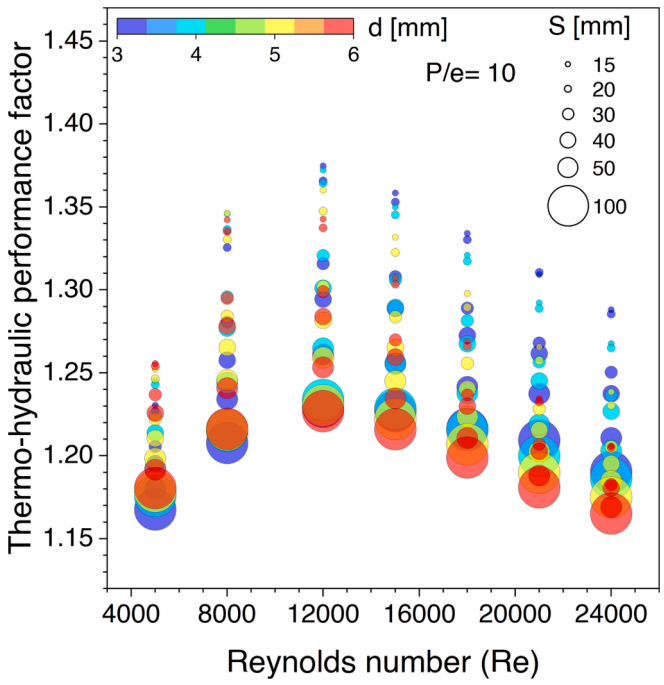

Fig. 10. The variation in the THPF values for different values of rib diameter.

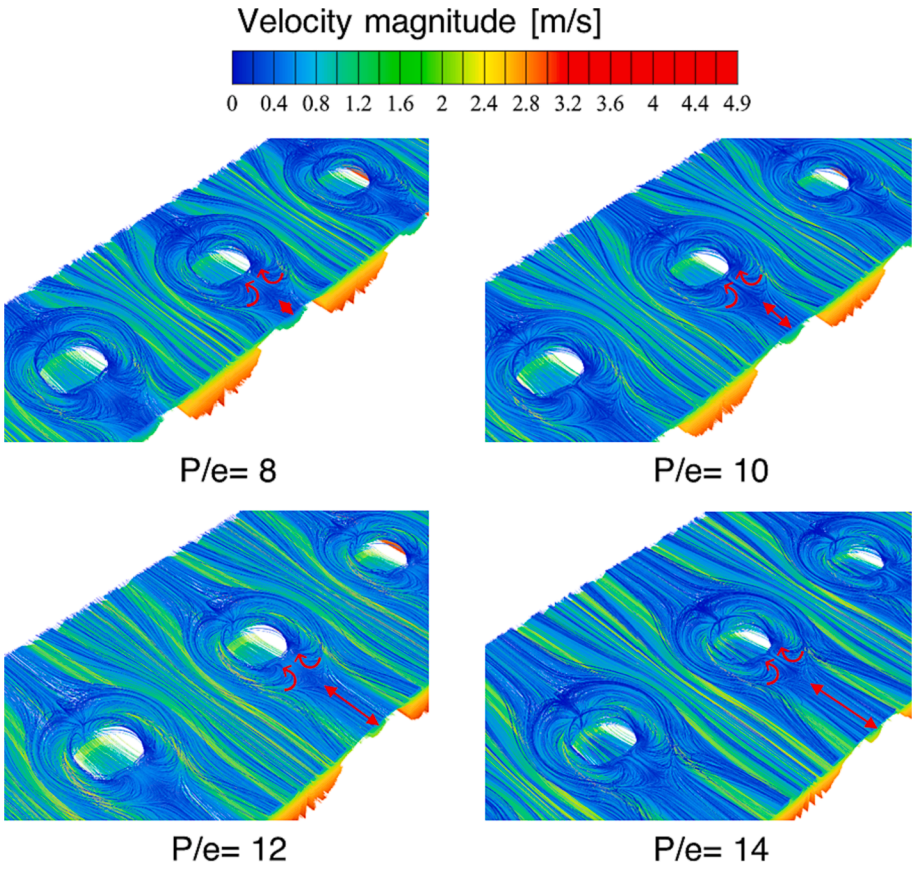

Fig. 9. The path lines coloured by velocity magnitude plotted for different values of P/e.

separated fluid particles are observed to undergo downward re-circulation in both clockwise and anticlockwise directions behind the cylindrical body, forming downstream re-circulation regions in the upper and lower halves of the cylindrical bodies along the fluid flow direction. These re-circulating flows effectively transfer heat from the absorber plate to the core fluid. The double arrow line defines the half reattachment length between the two straight ribs in the longitudinal direction, as illustrated in Fig. 9. Hence, based on this phenomenon, $P/e = 10$ is the optimum value found for maximum THPF amongst all the investigated values of the longitudinal pitch.

4.3.3. Effects of rib diameter (d)

After optimizing the longitudinal pitch in the preceding subsection, this section focuses on examining the impact of rib diameter with a constant value of $P/e = 10$. The variation of THPF is shown in Fig. 10 against the *Re* values. The rib diameter varies from 3 mm to 6 mm for CFD analysis. The variation in THPF is plotted for different values of rib diameter and the different values of the transverse pitch. The plot shows that the values attain maximum at $Re = 12000$ and start declining on increasing *Re* values. A similar trend is observed for all the values of the transverse pitch. Fig. 10 shows that the maximum THPF value of 1.37 is achieved for d = 3 mm, S = 15 mm at $Re = 12000$. Hence, it is concluded that the smaller rib diameter is the best in terms of maximizing THPF due to reduced obstruction within the duct.

Further, to understand the reason behind the optimum value for maximum THPF with a smaller rib diameter, the velocity contours are extracted from the CFD analysis for all the values of rib diameter at $Re = 12000$, which are represented in Fig. 11. These contours reveal that fluid particles, upon impact with the cylindrical surface in the flow direction, are separated to flow around the cylindrical body. The separated fluid particles subsequently mix with the remaining fluid stream, transferring the energy to the flowing fluid. However, as the rib diameter increases, a more pronounced wake region starts forming behind the cylindrical body, resulting in increased pressure drop within the duct. Despite the stream velocity rising between the ribs, the creation of back pressure in front of the cylindrical rib contributes to elevated pressure drop values within the duct. Therefore, it can be concluded that the smaller rib diameter effectively separates the fluid streams and provides ample space for heat transfer from the absorber plate. Thus, d = 3 mm is determined to be the optimum value for achieving maximum THPF.

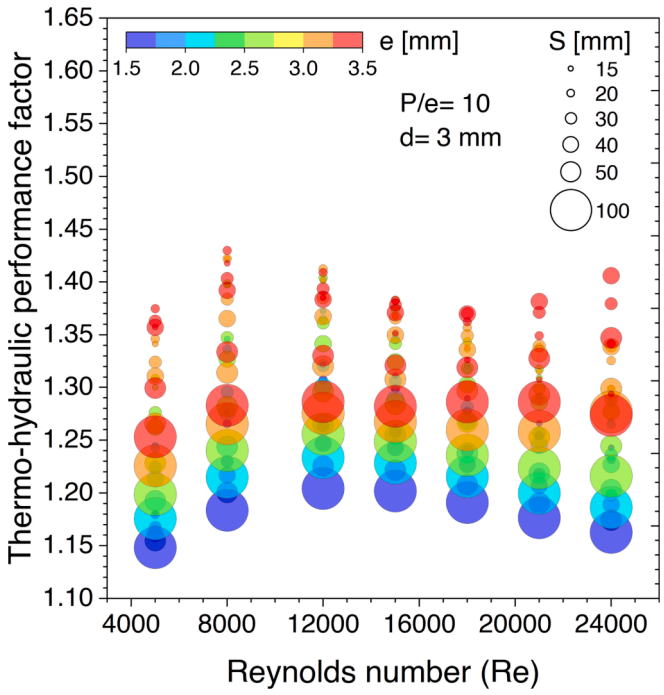

Fig. 12. The variation in THPF values against *Re* for different rib height values.

4.3.4. Effects of rib height (e)

Though the longitudinal pitch and the rib diameter are already optimized in the preceding subsections, the effects of rib height are highlighted in this section. Fig. 12 shows the variation of THPF value against the Reynolds number for different values of rib height. The rib height varies from 1.5 mm to 3.5 mm for a fixed optimized value of $P/e = 10$ and d = 3 mm. The effects of rib height are simulated for different values of the transverse pitch. It is observed from the plot that the THPF

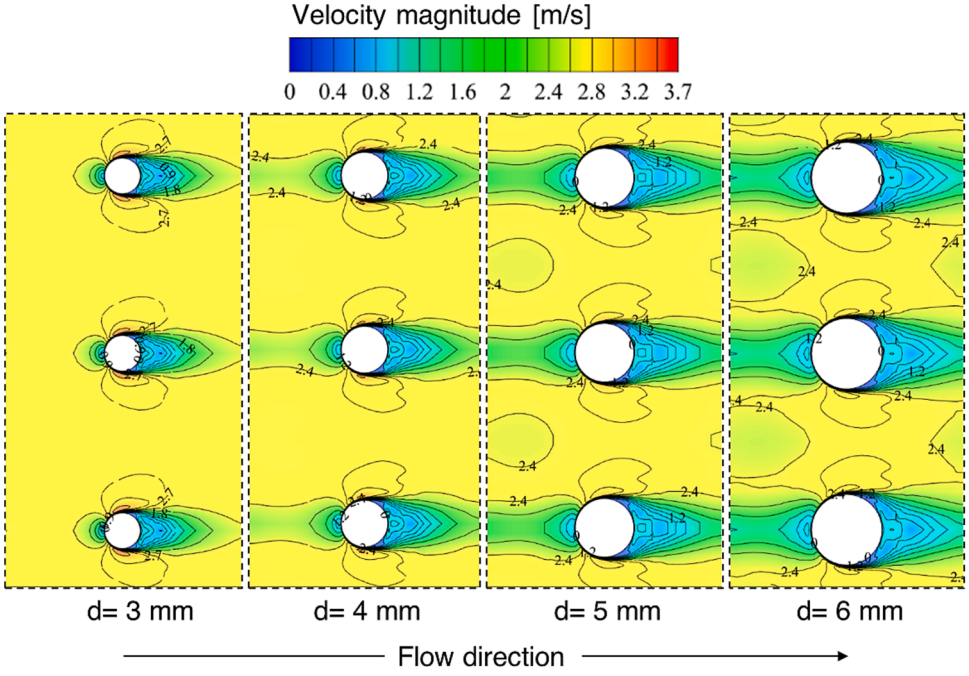

Fig. 11. Velocity contours for different values of rib diameter at 1 mm below the absorber plate.

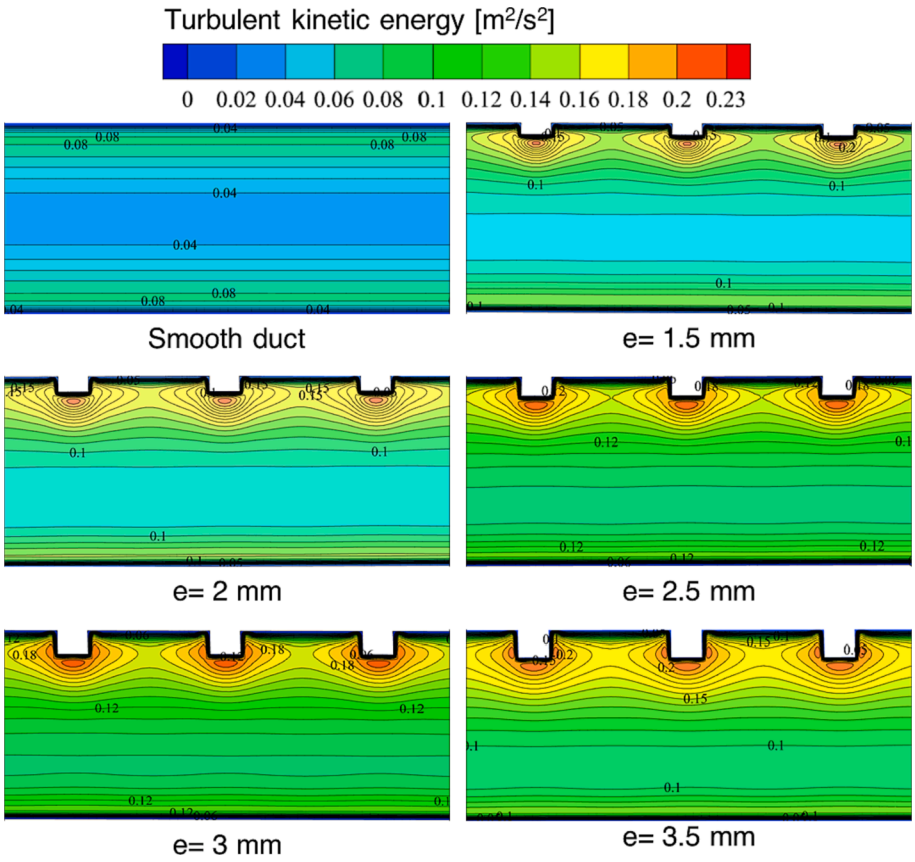

Fig. 13. The turbulent kinetic energy contours at the mid-plane of the computational fluid domain.

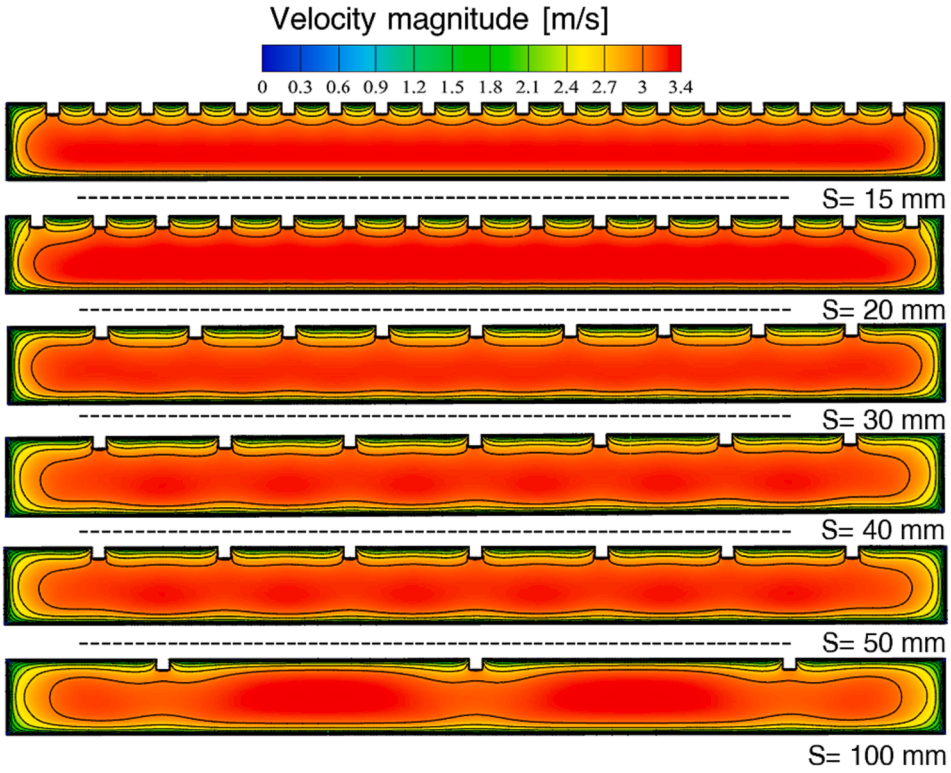

Fig. 14. The velocity contours at the mid-plane perpendicular to the absorber plate in the direction of fluid flow.

values increase on increasing the *Re* values and attains the maximum at *Re* = 8000. This trend is observed for all the values of the transverse pitch. The maximum THPF value is 1.43 yielded for e = 3.5, S = 20 mm, *P/e* = 10, and d = 3 mm at *Re* = 8000. Hence, e = 3.5 mm is the optimum value obtained for the maximum THPF value.

To substantiate the reasoning behind the maximum THPF value for these geometric values, the turbulent kinetic energy (TKE) contours are illustrated in Fig. 13. The TKE contours are extracted from the CFD analysis. By comparing these contours with those obtained from a smooth duct, the impact of rib height on TKE becomes apparent. In Fig. 13, the smooth duct exhibits maximum TKE values near the wall. This observation suggests that the introduction of artificial roughness, such as ribs, could lead to heightened TKE values. Therefore, as the ribs are installed beneath the absorber plate, they contribute to generating the highest levels of turbulent kinetic energy (TKE) in their immediate vicinity. Consequently, the intensity of TKE progressively amplifies in tandem with the increase in rib height. Moreover, the height of these ribs plays a role in influencing the TKE intensity along the lower wall of the duct. As rib height increases, a noteworthy phenomenon emerges: the peaks of TKE intensity start intersecting with one another, especially at higher rib heights. This occurrence underlines the rationale behind the enhanced thermal performance of ducts featuring roughened surfaces. The study shows that the maximum value of THPF is found with e = 3.5 mm. This phenomenon is attributed to the collision of the high-intensity peaks that are generated in the region around the cylindrical bodies located between the ribs, specifically in the transverse direction.

4.3.5. *Effects of transverse pitch (S)*

In addition to the longitudinal pitch, the vertical cylindrical ribs are also varied in the transverse direction and this length is denoted by the letter 'S'. The transverse pitch is varied from 15 mm to 100 mm for CFD analysis. Though, the parametric optimization of the geometric parameters is discussed in the preceding subsections for different values of the transverse pitch. The maximum THPF of 1.43 is achieved for S = 20 mm at *Re* = 8000; hence this is the optimum value for a transverse pitch.

Fig. 14 shows velocity contours for various transverse pitch values at *Re* = 8000, considering the optimized geometric topology of vertical cylindrical ribs. These velocity contours are extracted at the mid-plane of the computational fluid domain, oriented perpendicular to the absorber plate. It is observed that the distance between successive ribs in the transverse direction affects the intensity of the core fluid. As the transverse pitch varies from 15 mm to 100 mm, the core fluid starts shifting at the center of the computational fluid domain in the direction of fluid flow. This indicates the development of the viscous sublayer near the walls, leading to the reduction in the impact of the ribs attached to the wetted surface of the absorber plate. However, for larger transverse pitch values, the turbulence generated near the walls becomes relatively insignificant.

Hence, the lower values are observed to be effective in terms of the turbulence generated near the walls, as these combinations constantly disturb the fluid flow behaviour near the walls. This increases the pressure drop penalty in the computational fluid domain because of the obstruction produced in the fluid flow path. Therefore, these observations forced us to make a trade-off between these phenomena by varying the transverse pitch to get the maximum THPF. Hence, S = 20 mm is obtained to be the optimum value based on the velocity contours.

The impact of lower values of the transverse pitch on turbulence generated in close proximity to the walls is evident. However, this effect results in an increased pressure drop within the computational fluid domain due to the formation of obstructions in the fluid flow pathway. As a direct consequence of these observations, the need to strike a delicate equilibrium between these phenomena arose, prompting to consider adjusting the transverse pitch in order to achieve the maximum THPF.

Fig. 15 showcases turbulent intensity contours for various transverse pitch values at *Re* = 8000, focusing on the optimized geometric parameters for the vertical cylindrical ribs. These contours are extracted at the mid-plane of the computational fluid domain, perpendicular to the absorber plate. Turbulent intensity represents the root mean square of the turbulent velocity fluctuations in relation to the mean velocity, providing insights into the turbulence in specific zones. Analysis of the contours reveals that maximum turbulence intensity is located near the

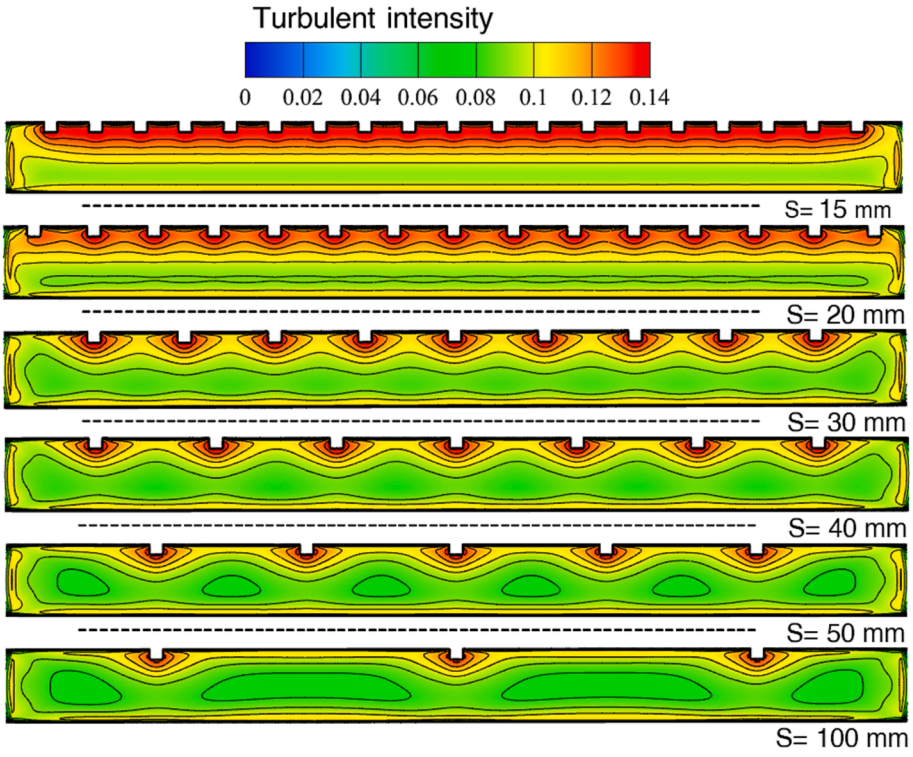

Fig. 15. The turbulent intensity contours at the mid-plane normal to the absorber plate in the direction of fluid flow.

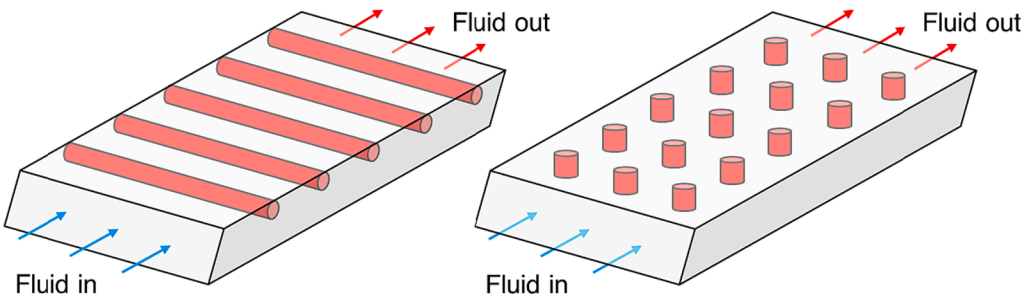

Fig. 16. CAD model of the ribs oriented in different directions to the absorber plate.

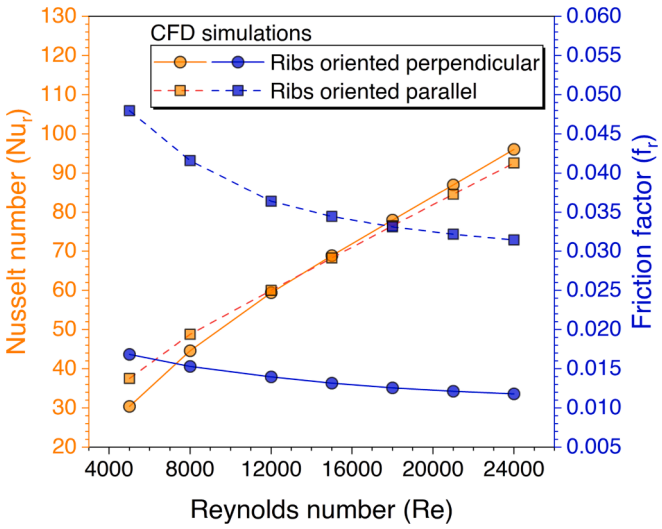

Fig. 17. The Nu$_r$ and f$_r$ values variation for different orientations of ribs.

ribs. In essence, the ribs induce turbulence near the absorber plate, resulting in enhanced heat transfer extraction. Nonetheless, with a transverse pitch value of S = 15 mm, turbulent intensities are excessively high, leading to increased frictional losses due to reduced spacing between consecutive ribs. While increasing the transverse pitch to 20 mm achieves a more balanced development of turbulent intensities near the ribs, reducing obstructions between consecutive ribs in the transverse direction. Consequently, this value is identified as the optimum choice for maximizing THPF.

4.4. Comparison between different orientations of the cylindrical ribs

The optimized ribs configuration is further explored with an orientation parallel to the absorber plate. The fundamental concept behind the model for both configurations is illustrated in Fig. 16. The optimized geometric parametric values of the cylindrical ribs are employed in both orientations to facilitate a relevant comparison. This investigation is carried out under identical operating conditions, and the results are presented in Fig. 17 for the purpose of comparison.

Fig. 17 shows the Nu_r and f_r values variation for different orientations of the cylindrical ribs. The Nusselt number values exhibit an increase as *Re* values increases, while the friction factor values decrease with increasing *Re* values. Furthermore, Nusselt number values for the orientation perpendicular to the absorber plate surpass those for the orientation parallel to the absorber plate beyond *Re* = 15000. In both orientations, friction factor values decrease as *Re* increases. The friction factor values are significantly lower with the ribs oriented perpendicular to the absorber plate—roughly one-third of those with ribs oriented

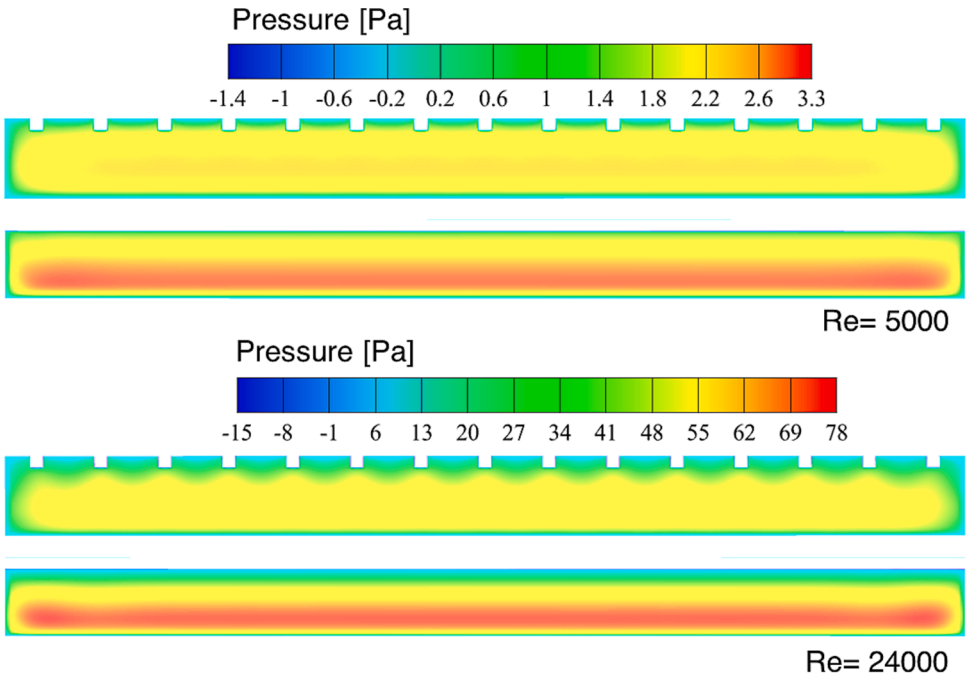

Fig. 18. Pressure contours for different orientations of cylindrical ribs at the mid-plane perpendicular to the absorber plate.

parallel to the absorber plate. This discussion concludes that ribs oriented perpendicular to the absorber plate perform better in terms of both Nusselt number and friction factor values, attributed to the discrete nature of the cylindrical ribs.

Further, to understand the reason behind the increased friction factor associated with cylindrical ribs aligned parallel to the absorber plate as compared to the perpendicular orientation, pressure contours are extracted at the mid-plane perpendicular to the absorber plate for the lower and higher range of the Reynolds number (shown in Fig. 18). Upon analyzing the pressure contours, a significant insight emerges. The continuous arrangement of cylindrical ribs, when oriented parallel to the absorber plate, leads to an increase in pressure drop. Conversely, when the cylindrical ribs are positioned perpendicular to the absorber plate, the pressure drop is notably lower. In simpler terms, the discrete arrangement of vertical cylindrical ribs creates sufficient space for fluid flow to progress smoothly in the downstream region. In contrast, the presence of continuous cylindrical ribs obstructs fluid flow, resulting in a heightened pressure drop within the test section.

4.5. Comparison of CFD results with experimental results

The experimental validation is conducted on a roughened duct, employing the same geometric conditions considered in the CFD investigation. The experimental values are graphed alongside the CFD simulation results, as depicted in Fig. 19. To account for uncertainty, each experimental value is presented with an associated uncertainty bar calculated for each *Re*. The same trend is observed in the experimental values as in the CFD simulation results on increasing the Reynolds number. Details regarding the uncertainty range for each value are provided in **Appendix A**. Also, the experimental Nusselt number values were in agreement with the CFD values and the Gnielinski correlation for smooth duct. However, a noticeable discrepancy arises in the case of Nusselt number values for the roughened duct. These values appear to fall short in comparison to the numerical values derived from CFD simulations. The underlying cause can be attributed to the challenge of completely insulating the experimental duct, despite thorough wrapping with insulating material.

4.6. Effects of rotating ribs (N)

To mitigate the formation of re-circulation zones on either side of the fixed artificial roughness, a novel concept involving rotating ribs has been studied, utilizing the optimized configuration of static cylindrical ribs. These ribs rotate counter to the incoming fluid flow, with rotational speeds ranging from 2000 RPM to 10,000 RPM. The Nusselt number and friction factor values are extracted from the CFD investigation and compared with the smooth and roughened duct values.

Fig. 20 reveals that Nusselt number values increase with increase in Reynolds numbers and rotational speed of the ribs. A similar pattern is apparent in both the smooth and roughened duct configurations with fixed ribs as Reynolds numbers increase. However, it's particularly noteworthy that the introduction of rotating ribs leads to a significant improvement in Nusselt number values compared to stationary ribs. This enhancement can be attributed to the enhanced mixing of stagnant fluid particles within re-circulation zones with primary fluid particles, driven by the counter-rotation of the ribs against the incoming flow, as shown in Fig. 21.

Additionally, this enhanced mixing phenomenon can be linked to the mechanism that in the case of fixed cylinders, the fluid is evenly divided upon striking the ribs in the direction of the fluid flow and subsequently mingles with the surrounding fluid within the spaces between the ribs. In contrast, the presence of rotating ribs alters the separation angle by shifting it in an upward direction (can be seen in Fig. 21). This shift is a result of the increased adherence of fluid particles to the cylindrical bodies, a phenomenon facilitated by the rotational speed of the ribs. Consequently, fluid particles exhibit a higher propensity for attachment

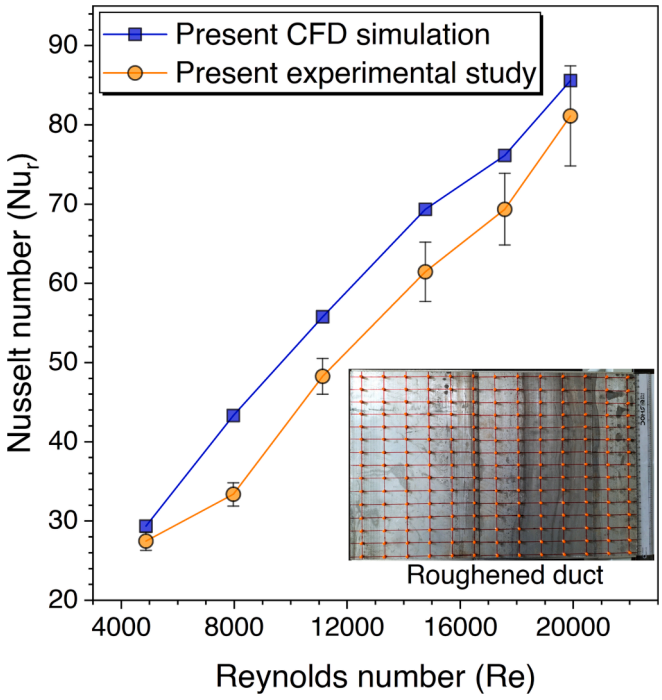

Fig. 19. Experimental validation for the roughened duct with the optimized vertical cylindrical ribs.

under rotational conditions, resulting in an elevated heat capture from the absorber plate. This, in turn, leads to an enhancement in the Nusselt number. Remarkably, the maximum Nusselt number values are achieved at a rotational speed of 10,000 RPM for all Reynolds number.

In order to gain a deeper understanding of the fluid flow and heat transfer characteristics involving rotating ribs as compared to fixed ribs, velocity, and temperature contours have been plotted in the direction perpendicular to the absorber plate's surface (see Fig. 22). These contours provide insights into how the fluid behaves within this

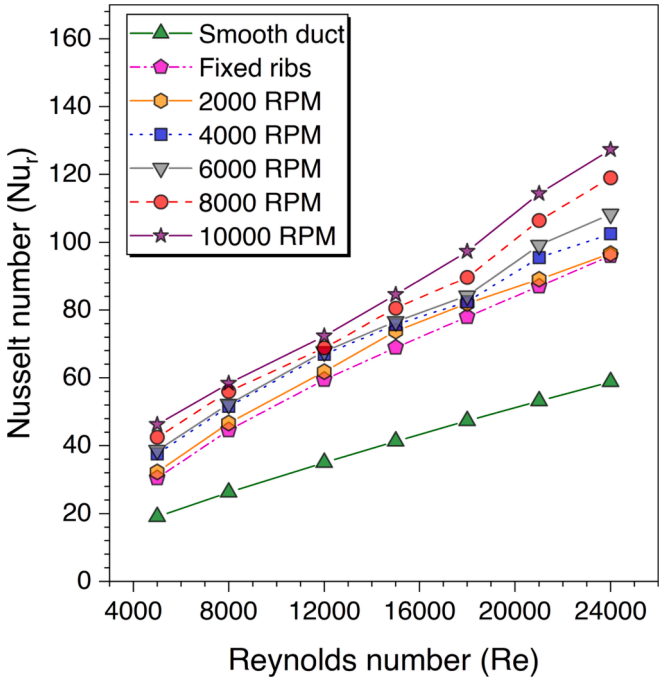

Fig. 20. The Nusselt number values variation against the Reynolds number for different rotational speeds.

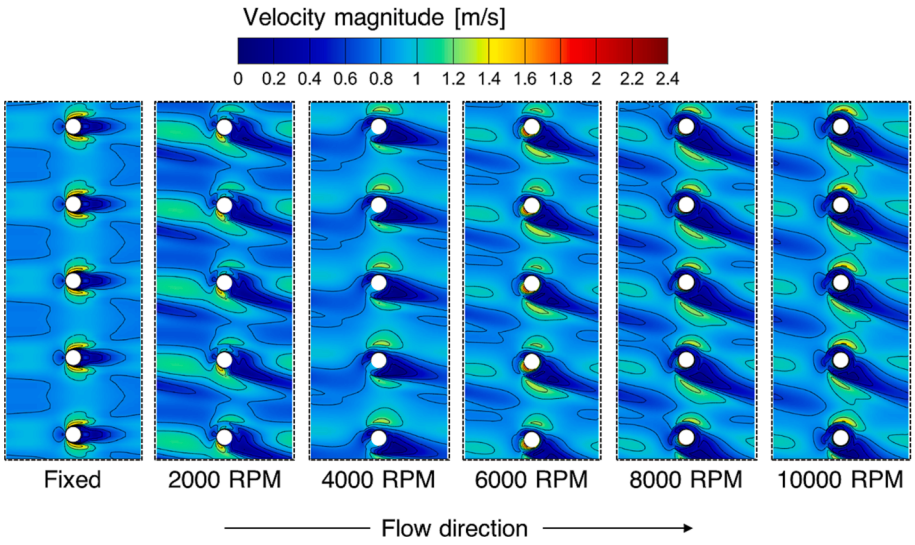

Fig. 21. Velocity contours at a plane 1 mm below the absorber plate for fixed and rotating ribs.

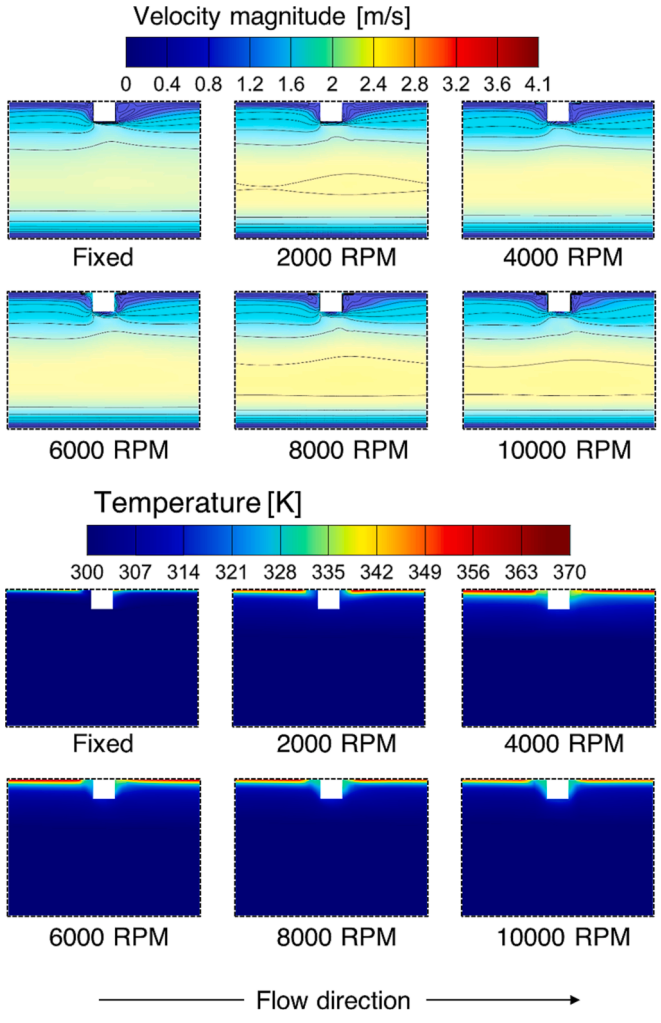

Fig. 22. The velocity and temperature contours at a plane normal to the absorber plate.

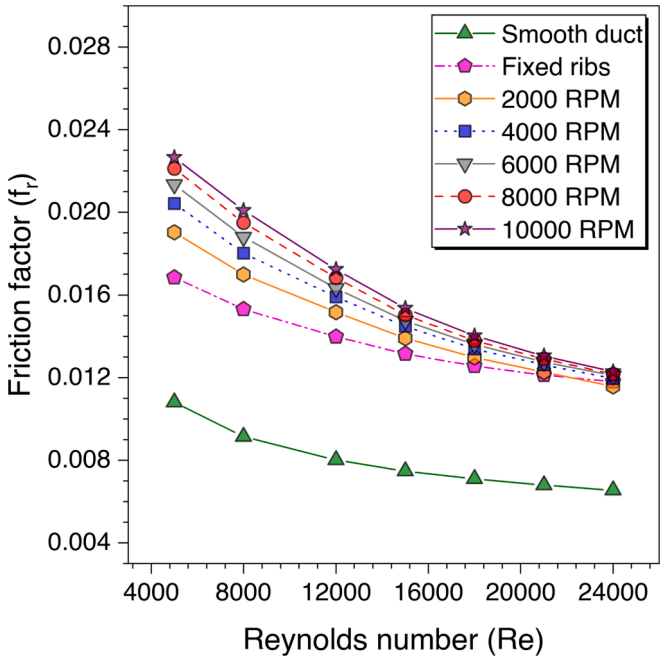

Fig. 23. The friction factor values variation against the Reynolds number for different rotational speeds.

configuration. Upon analysis, it becomes evident that the presence of rotating ribs has a distinct impact on the fluid flow. Specifically, the fluid particles that would typically become trapped behind fixed ribs are now less prone to stagnation due to the absence of circulation zones created by the rotating ribs. This shift leads to a continuous interaction of the fluid particles with the primary fluid stream. Consequently, there is an efficient transfer of heat from the absorber plate. Furthermore, the temperature contours also underscore the amplified heat transfer effects in the system especially being more pronounced in proximity to the absorber plate. This signifies that the arrangement of rotating ribs not only influences fluid flow behavior but also positively impacts heat distribution and transfer, resulting in improved overall performance.

Further, Fig. 23 shows the friction factor values variation against the Reynolds number values for different rotational speeds. The friction

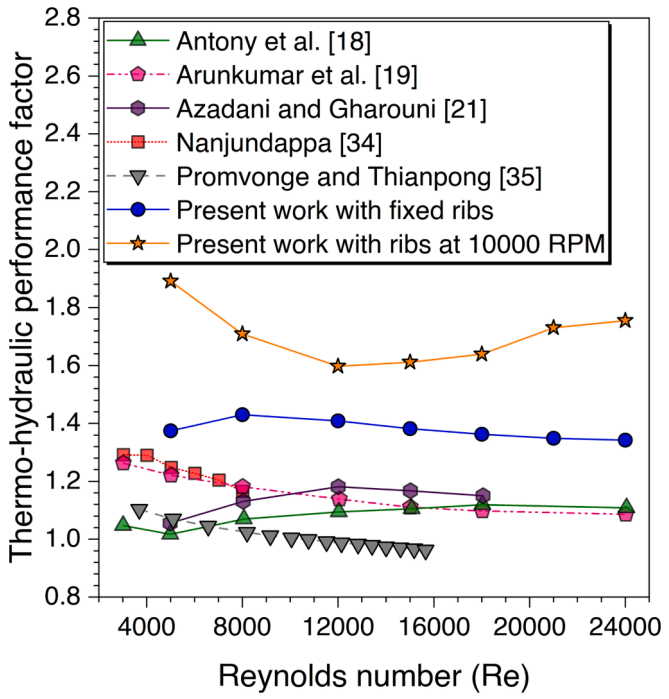

Fig. 24. Comparison with works available in the literature.

factor values are observed to be decreasing with increasing the Reynolds number values for all the investigated rotational speeds, whereas the friction factor values increase on increasing the rotational speed of the cylindrical ribs at a particular Reynolds number. The friction factor values are also observed to converge to a value at $Re = 24000$, which means the rotational speed is becoming insignificant for friction factor at a higher Reynolds number. In other words, the friction factor values with rotational cylindrical ribs were the same as with the fixed cylindrical ribs at $Re = 24000$.

4.7. Comparison with research works in the literature

The THPF of the present case is compared with the other studies conducted under the same orientation of the ribs but with different cross-sectional ribs in Fig. 24. The maximum THPF values are chosen for comparison against the THPF values of present study. Various rib configurations, including cubical [34], helicoidal spring-shaped fins [19], stepped cylinders [18,21], cylindrical shape [21], and wedge-shaped right-triangular [35] cross-sections, are considered. The results from the present arrangement of fixed vertical cylindrical ribs are observed to surpass the other's work available in the literature with different configurations within the same orientation. Furthermore, the thermal performance achieved with the rotating ribs outperforms even the present combination of vertical fixed cylindrical ribs. The highest THPF value of 1.89 is recorded at $Re = 5000$ with a rotational speed of $N = 10000$ RPM.

5. Conclusions

A novel concept of rotating cylindrical ribs as artificial roughness in a solar air heater to enhance its thermo-hydraulic performance factor has been investigated using 3D computational fluid dynamics. The cylindrical ribs rotate counter to the incoming fluid flow, with rotational speeds ranging from 2000 RPM to 10,000 RPM. Parametric optimization is performed using static vertical cylindrical ribs with for geometric parameters defined by rib diameter (d), and rib height (e), longitudinal pitch (P), and transverse pitch (S). Rib diameter varies from 3 mm to 6 mm, while rib height varies from 1.5 mm to 3.5 mm. Longitudinal pitch is expressed as a dimensionless parameter called relative roughness pitch (P/e) and varied from 8 to 14. The effects of these parameters are assessed against Reynolds numbers, spanning 5000 to 24000, and optimized outcomes are determined based on the maximum thermo-hydraulic performance factor value. Additionally, an experimental investigation is conducted for both smooth and roughened ducts, facilitating comparison with CFD-derived results. The major outcomes of this research work are:

- The highest THPF value of 1.43 is achieved at $Re = 8000$ for e = 3.5 mm, d = 3 mm, S = 20 mm, and $P/e = 10$ for static cylindrical ribs oriented perpendicular with respect to the absorber plate.
- The optimized perpendicular discrete cylindrical ribs are also evaluated against the parallel cylindrical ribs. The Nusselt number values with vertical cylindrical ribs are observed to surpass the latter arrangement after $Re = 15000$, however, the friction factor values are found to be significantly less with vertical cylindrical ribs in comparison to the transverse cylindrical ribs for all values of Reynolds number.
- The maximum Nusselt number of 127.37 is attained for optimized geometry at $Re = 24000$ and N = 10000 RPM.
- Friction factor values decrease with increasing Reynolds numbers for each rotational speed, converging at $Re = 24000$. However, the peak friction factor of 0.0267 is achieved at $Re = 5000$ for N = 10000 RPM.
- The maximum thermo-hydraulic performance factor of 1.89 is achieved—32 % higher than the best performance for static ribs—using rotational ribs for the rotational speed of 10,000 RPM at $Re = 5000$.

Funding

This research did not receive any specific grant from funding agencies in the public, commercial, or not-for-profit sectors.

CRediT authorship contribution statement

Sarvapriya Singh: Methodology, Software, Investigation, Data curation, Formal analysis, Writing – original draft. **Siddharth Suman:** Investigation, Supervision, Visualization, Writing – original draft, Writing – review & editing. **Santanu Mitra:** Supervision, Resources. **Manish Kumar:** Supervision, Writing – review & editing.

Declaration of Competing Interest

The authors declare that they have no known competing financial interests or personal relationships that could have appeared to influence the work reported in this paper.

Data availability

No data was used for the research described in the article.

Appendix A. Supplementary material

Supplementary data to this article can be found online at https://doi.org/10.1016/j.applthermaleng.2023.121748.

References

[1] S. Suman, K. Mohd, M.P. Khan, Performance enhancement of solar collectors—A review, Renew. Sustain. Energy Rev. 49 (2015) 192–210, https://doi.org/10.1016/J.RSER.2015.04.087.
[2] S. Suman, Hybrid nuclear-renewable energy systems: A review, J. Clean. Prod. 181 (2018) 166–177, https://doi.org/10.1016/J.JCLEPRO.2018.01.262.
[3] S. Singh, S. Suman, S. Mitra, M. Kumar, Solar air heater with rotating circular ribs: Hybrid CFD-ANN approach for prediction of thermo-hydraulic performance, Energy Rep. 8 (2022) 145–150, https://doi.org/10.1016/J.EGYR.2022.10.084.

[4] S. Singh, S. Suman, S. Mitra, M. Kumar, ANN model for prediction of thermo-hydraulic performance of a solar air heater with vertical cylindrical ribs, Energy Rep. 8 (2022) 585–592, https://doi.org/10.1016/J.EGYR.2022.10.263.
[5] M. Sheikholeslami, Numerical investigation of solar system equipped with innovative turbulator and hybrid nanofluid, Sol. Energy Mater. Sol. Cells 243 (2022), 111786, https://doi.org/10.1016/J.SOLMAT.2022.111786.
[6] M. Sheikholeslami, M. Jafaryar, Thermal assessment of solar concentrated system with utilizing CNT nanoparticles and complicated helical turbulator, Int. J. Therm. Sci. 184 (2023), 108015, https://doi.org/10.1016/J.IJTHERMALSCI.2022.108015.
[7] J. Williamson, Laws of flow in rough pipes, Houille Blanche (1951) 738–757, https://doi.org/10.1051/lhb/1951058.
[8] R.L. Webb, E.R.G. Eckert, R.J. Goldstein, Heat transfer and friction in tubes with repeated-rib roughness, Int. J. Heat Mass Transf. 14 (1971) 601–617, https://doi.org/10.1016/0017-9310(71)90009-3.
[9] R.L. Webb, E.R.G. Eckert, R.J. Goldstein, Generalized heat transfer and friction correlations for tubes with repeated-rib roughness, Int. J. Heat Mass Transf. 15 (1972) 180–184, https://doi.org/10.1016/0017-9310(72)90179-2.
[10] R.L. Webb, E.R.G. Eckert, Application of rough surfaces to heat exchanger design, Int. J. Heat Mass Transf. 15 (1972) 1647–1658, https://doi.org/10.1016/0017-9310(72)90095-6.
[11] K. Prasad, S.C. Mullick, Heat transfer characteristics of a solar air heater used for drying purposes, Appl. Energy 13 (1983) 83–93, https://doi.org/10.1016/0306-2619(83)90001-6.
[12] J.S. Prasad, B.N. Saini, Effect of artificial roughness on heat transfer and friction factor in a solar air heater, Sol. Energy 41 (1988) 555–560.
[13] D. Gupta, S.C. Solanki, J.S. Saini, Heat and fluid flow in rectangular solar air heater ducts having transverse rib roughness on absorber plates, Sol. Energy 51 (1993) 31–37, https://doi.org/10.1016/0038-092X(93)90039-Q.
[14] S.K. Verma, B.N. Prasad, Investigation for the optimal thermohydraulic performance of artificially roughened solar air heaters, Renew. Energy 20 (2000) 19–36, https://doi.org/10.1016/S0960-1481(99)00081-6.
[15] V.B. Gawande, A.S. Dhoble, D.B. Zodpe, S. Chamoli, A review of CFD methodology used in literature for predicting thermo-hydraulic performance of a roughened solar air heater, Renew. Sustain. Energy Rev. 54 (2016) 550–605, https://doi.org/10.1016/j.rser.2015.10.025.
[16] M.S. Manjunath, K.V. Karanth, N.Y. Sharma, Numerical analysis of the influence of spherical turbulence generators on heat transfer enhancement of flat plate solar air heater, Energy 121 (2017) 616–630, https://doi.org/10.1016/j.energy.2017.01.032.
[17] M.S. Manjunath, K. Vasudeva Karanth, N. Yagnesh Sharma, Numerical analysis of flat plate solar air heater integrated with an array of pin fins on absorber plate for enhancement in thermal performance, J. Solar Energy Eng. Trans. ASME 141 (2019), https://doi.org/10.1115/1.4043517.
[18] A.L. Antony, S.P. Shetty, N. Madhwesh, N. Yagnesh Sharma, K. Vasudeva Karanth, Influence of stepped cylindrical turbulence generators on the thermal enhancement factor of a flat plate solar air heater, Sol. Energy 198 (2020) 295–310, https://doi.org/10.1016/j.solener.2020.01.065.
[19] H.S. Arunkumar, S. Kumar, K.V. Karanth, Analysis of a solar air heater for augmented thermohydraulic performance using helicoidal spring shaped fins-A numerical study, Renew. Energy 160 (2020) 297–311, https://doi.org/10.1016/j.renene.2020.06.098.
[20] M. Jovani, M. Khoshvaght-Aliabadi, M.M. Rashidi, Effects of vertical coil springs on the performance of solar air heaters: Experimental study, Appl. Therm. Eng. 230 (2023), 120701, https://doi.org/10.1016/j.applthermaleng.2023.120701.
[21] L.N. Azadani, N. Gharouni, Multi objective optimization of cylindrical shape roughness parameters in a solar air heater, Renew. Energy 179 (2021) 1156–1168, https://doi.org/10.1016/j.renene.2021.07.084.
[22] A. Chaube, P.K. Sahoo, S.C. Solanki, Analysis of heat transfer augmentation and flow characteristics due to rib roughness over absorber plate of a solar air heater, Renew. Energy 31 (2006) 317–331, https://doi.org/10.1016/j.renene.2005.01.012.
[23] S. Kumar, R.P. Saini, CFD based performance analysis of a solar air heater duct provided with artificial roughness, Renew. Energy 34 (2009) 1285–1291, https://doi.org/10.1016/j.renene.2008.09.015.
[24] S. Singh, B. Singh, V.S. Hans, R.S. Gill, CFD (computational fluid dynamics) investigation on Nusselt number and friction factor of solar air heater duct roughened with non-uniform cross-section transverse rib, Energy 84 (2015) 509–517, https://doi.org/10.1016/j.energy.2015.03.015.
[25] D.S. Thakur, M.K. Khan, M. Pathak, Performance evaluation of solar air heater with novel hyperbolic rib geometry, Renew. Energy 105 (2017) 786–797, https://doi.org/10.1016/j.renene.2016.12.092.
[26] I. Singh, S. Singh, CFD analysis of solar air heater duct having square wave profiled transverse ribs as roughness elements, Sol. Energy 162 (2018) 442–453, https://doi.org/10.1016/j.solener.2018.01.019.
[27] A. Kumar, A. Layek, Nusselt number and fluid flow analysis of solar air heater having transverse circular rib roughness on absorber plate using LCT and computational technique, 14, 2019.
[28] R.K.B. Gallegos, R.N. Sharma, Flags as vortex generators for heat transfer enhancement: Gaps and challenges, Renew. Sustain. Energy Rev. 76 (2017) 950–962, https://doi.org/10.1016/j.rser.2017.03.115.
[29] S. Rashidi, M. Hossein Kashefi, F. Hormozi, Potential applications of inserts in solar thermal energy systems – A review to identify the gaps and frontier challenges, Sol. Energy 171 (2018) 929–952, https://doi.org/10.1016/j.solener.2018.07.017.
[30] S. Singh, S. Mitra, M. Kumar, S. Suman, Thermal performance evaluation of a solar air heater with rotating turbulators, Sustain. Energy Technol. Assess. 48 (2021), 101647, https://doi.org/10.1016/J.SETA.2021.101647.
[31] S. Singh, S. Suman, S. Mitra, M. Kumar, Optimization of a novel trapezoidal staggered ribs configuration for enhancement of a solar air heater performance using CFD, Environ. Sci. Pollut. Res. 2023 (1) (2023) 1–20, https://doi.org/10.1007/S11356-023-28978-9.
[32] D. Taler, Experimental determination of correlations for average heat transfer coefficients in heat exchangers on both fluid sides, Heat Mass Transfer/waerme-Und Stoffuebertragung. 49 (2013) 1125–1139, https://doi.org/10.1007/s00231-013-1148-5.
[33] S. Singh, S. Mitra, M. Kumar, S. Suman, Thermal performance evaluation of a solar air heater with rotating turbulators, Sustain. Energy Technol. Assess. 48 (2021), https://doi.org/10.1016/j.seta.2021.101647.
[34] M. Nanjundappa, Optimum thermo-hydraulic performance of solar air heater provided with cubical roughness on the absorber surface, Exp. Heat Transfer 33 (2020) 374–387, https://doi.org/10.1080/08916152.2019.1652214.
[35] P. Promvonge, C. Thianpong, Thermal performance assessment of turbulent channel flows over different shaped ribs, Int. Commun. Heat Mass Transfer 35 (2008) 1327–1334, https://doi.org/10.1016/j.icheatmasstransfer.2008.07.016.